



Milestone Report

CFD Study of Countercurrent Flow in Triply Periodic Minimal Surfaces with CO₂BOL Solvent

Work Performed Under

Activity Number 0004000.6.600.007.002 ARRA

Prepared by

Pacific Northwest National Laboratory

Richland, Washington 99352

Prepared for the

U.S. Department of Energy

National Energy Technology Laboratory

December 2019



Revision Log

Revision	Date	Revised By:	Description
0.1	12/22/2019	Yucheng Fu	Initial Draft
0.2	01/08/2020	Yucheng Fu and Zhijie Xu	Revision with formatting
0.3	01/10/2020	Grigorios Panagakos	Revision with formatting

Disclaimer

This report was prepared as an account of work sponsored by an agency of the United States government. Neither the United States government nor any agency thereof, nor any of their employees, makes any warranty, express or implied, or assumes any legal liability or responsibility for the accuracy, completeness, or usefulness of any information, apparatus, product, or process disclosed, or represents that its use would not infringe privately owned rights. Reference herein to any specific commercial product, process, or service by trade name, trademark, manufacturer, or otherwise does not necessarily constitute or imply its endorsement, recommendation, or favoring by the United States government or any agency thereof. The views and opinions of authors expressed herein do not necessarily state or reflect those of the United States government or any agency thereof.

Acknowledgment of Funding

This project was funded under the Carbon Capture Simulation for Industry Impact (CCSI²) under the following FWP and contracts:

PNNL – 29590

Contents

Nomenclature..... 6

Acronyms 7

Executive Summary..... 8

1 Background 9

2 Methodology 10

 2.1 Geometries 10

 2.2 Mathematical Formulations..... 14

 2.3 Simulation Setup and Boundary Conditions..... 15

3 Results and Discussions..... 18

 3.1 Gyroid Results..... 18

 3.2 Schwarz-D Results 20

 3.3 Schwarz-P Results..... 22

 3.4 Discussion and Analysis of Results. 24

4 Conclusions 26

5 Future Work 27

6 References 28

List of Figures

Fig. 2.1 Shape of three TPMS structure packing walls (a) Gyroid, (b) Schwarz-D and (c) Schwarz-P used in this study.	10
Fig. 2.2 Examples of creating two independent flow channels from the TPMS structure by subtracting the geometry walls.	12
Fig. 2.3 Comparison of specific area a_p and hydraulic diameter d_h of Gyroid, Schwarz-D, and Schwarz-P.	13
Fig. 2.4 (a) Schematic of the simulation setup using the Gyroid flow region as an example. The solvent is driven by gravity and an upward body force is applied to the gas phase. (b) The initial liquid film distribution visualized at the vertical cross-section plane ($y = 1$ cm) for a 2-cm unit size Gyroid.	16
Fig. 2.5 Transient plot of (a) liquid flow rate and (b) interface/wetted area in the 1 cm Schwarz-D structure with the initial liquid film thickness of 0.7 mm.	17
Fig. 3.1 Flow pattern visualization with 1-cm unit size Gyroid at vertical cross-section plan $y = 0.5$ cm and solvent flow rate of (a) $u_L = 7.37E-03$, (b) $2.46E-2$, and (c) $4.32E-2$ m/s.	19
Fig. 3.2 Flow pattern visualization with 2-cm unit size Gyroid at vertical cross-section plan $y = 0.5$ cm and solvent flow rate of (a) $u_L = 5.07E-03$, (b) $3.92E-2$, and (c) $9.65E-2$ m/s.	20
Fig. 3.3 Flow pattern visualization with 1-cm unit size Schwarz-D at vertical cross-section plan $y = 1$ cm and solvent flow rate of (a) $u_L = 1.29E-03$, (b) $1.77E-2$, and (c) $5.53E-2$ m/s.	21
Fig. 3.4 Flow pattern visualization of 2-cm unit size Schwarz-D at vertical cross-section plan $y = 2$ cm and solvent flow rate of (a) $u_L = 3.45E-03$, (b) $5.64E-2$, and (c) $7.59E-2$ m/s.	22
Fig. 3.5 Flow pattern visualization of 1-cm unit size Schwarz-P at vertical cross-section plan $y = 0.5$ cm and solvent flow rate of (a) $u_L = 1.07E-02$, (b) $1.61E-2$, and (c) $5.68E-2$ m/s.	23
Fig. 3.6 Flow pattern visualization of 2-cm unit size Schwarz-P at vertical cross-section plan $y = 1$ cm and solvent flow rate of (a) $u_L = 3.21E-03$, (b) $2.46E-2$, and (c) $8.635E-2$ m/s.	24
Fig. 3.7 Comparison of how the geometry size affects the normalized interfacial area $a_{i, \text{norm}}$ for (a) Gyroid, (b) Schwarz-D, and (c) Schwarz-P.	25
Fig. 3.8 Comparison of how the geometry size affects the interfacial area a_i for (a) Gyroid, (b) Schwarz-D, and (c) Schwarz-P.	25
Fig. 3.9 Comparison of the interfacial area a_i among Gyroid, Schwarz-D, and Schwarz-P with (1) 1-cm unit size geometry and (2) 2-cm unit size geometry.	25

List of Tables

Table 2.1 Summary of geometry properties of 1-cm and 2-cm unit size Gyroid, Schwarz-D, and Schwarz-P.....	13
Table 2.2 Summary of solvent and gas physical properties.....	16
Table 3.1 Summary of simulation results with 1-cm unit size Gyroid with $a_p = 613.76 \text{ m}^2/\text{m}^3$	19
Table 3.2 Summary of simulation results with 2-cm unit size Gyroid with $a_p = 306.84 \text{ m}^2/\text{m}^3$	20
Table 3.3 Summary of simulation results with 1-cm unit size Schwarz-D with $a_p = 748.02 \text{ m}^2/\text{m}^3$	21
Table 3.4 Summary of simulation results with 2-cm unit size Schwarz-D with $a_p = 374.10 \text{ m}^2/\text{m}^3$	22
Table 3.5 Summary of simulation results with 1-cm unit size Schwarz-P with $a_p = 467.38 \text{ m}^2/\text{m}^3$	23
Table 3.6 Summary of simulation results with 2-cm unit size Schwarz-P with $a_p = 233.71 \text{ m}^2/\text{m}^3$	24

Nomenclature

English

A_{cross}	Cross-section plane area [m ²]
a_i	Interfacial area concentration [m ² /m ³]
a_p	Specific area [m ² /m ³]
a_w	Wetted area concentration [m ² /m ³]
d_h	Hydraulic diameter [m]
d_p	Particle diameter [m]
g	Gravity [m/s ²]
p	Pressure [Pa]
Q	Liquid flow rate [m ³ /s]
t	Time [s]
u_g	Gas superficial velocity in packed column [m/s]
u_L	Liquid superficial velocity in packed column [m/s]
V	Total occupied volume [m ³]

Greek Letter

κ	Curvature of local surface/interface [1/m]
ϵ	Packing Porosity [-]
μ_g	Viscosity of gas [Pa·s]
μ_l	Viscosity of liquid [Pa·s]
ρ_g	Density of gas [kg/m ³]
ρ_l	Density of liquid [kg/m ³]
∇	Gradient operator [m ⁻¹]
α	Volume fraction of liquid [-]
σ	Surface tension [m/s]

SUBSCRIPT

c	Cross-section plane
g	Gas
i	Interface
l	Liquid
$norm$	Normalized
$offset$	Offset
p	Particle
w	Wetted

Acronyms

AM	additive manufacturing
CFD	computational fluid dynamics
CFL	Courant–Friedrichs–Lewy
CCSI ²	Carbon Capture Simulation for Industry Impact
CO ₂	carbon dioxide
CO ₂ BOL	CO ₂ binding organic liquids
HPC	high performance computing
HRIC	high-resolution interface capturing
LLNL	Lawrence Livermore National Laboratory
MEA	monoethanolamine
PIC	PNNL Institutional Computing
PNNL	Pacific Northwest National Laboratory
SIMPLE	Semi-Implicit Method for Pressure-Linked Equations
TPMS	triply periodic minimal surface
VOF	volume of fluid method

CFD Study of Countercurrent Flow in Triply Periodic Minimal Surfaces with CO₂BOL Solvent

Yucheng Fu, Jie Bao, Chao Wang, Rajesh Kumar Singh and Zhijie Xu
Pacific Northwest National Laboratory, Richland, WA 99352, USA

Grigorios Panagakos
National Energy Technology Laboratory, Pittsburgh, PA 15236, USA

Executive Summary

Triply periodic minimal surfaces (TPMS) are promising structures for heat exchangers and ultrafiltration due to their high heat and mass transfer efficiency compared to traditional devices. Because of this, the TPMS structures are a potential candidate for building the multifunctional, intensified devices in CO₂ capture tasks. With the Lawrence Livermore National Laboratory's (LLNL's) additive manufacturing (AM) capability, these complicated TPMS structures can be printed in the packed column for experimental tests. To optimize the TPMS structure and enable fast prototyping, a computationally-efficient computational fluid dynamics (CFD) framework was established to explore the TPMS structure's hydrodynamics and mass transfer performance. The established model was able to simulate the countercurrent flows by integrating the Pacific Northwest National Laboratory (PNNL) CO₂ binding organic liquids (CO₂BOL) solvent into the TPMS structures. Three typical TPMS structures—namely, Gyroid, Schwarz-D, and Schwarz-P—were investigated using the periodic boundary set up in all three directions. Two different unit cell size (1 cm and 2 cm) geometries are tested for each type of TPMS. The solvent flow rate in this study covered a range of [0, 0.1] m/s with an initial liquid film thickness of [0.1, 1.8] mm. These simulations provided a preliminary understanding of the TPMS structure behaviors in countercurrent flow conditions. The study also related the TPMS geometry requirement to the given CO₂BOL solvent physical properties and covered reasonable packed column operation ranges.

1 Background

Packed column is widely used for post-combustion CO₂ capture. Various structures and random packings have been developed in the packed column to provide an enhanced gas-liquid interface area for mass transfer[1]. Recent studies found that the triply periodic minimal surface (TPMS) structures can have improved efficiency in applications such as heat exchangers[2] and ultrafiltration[3], [4] when compared to traditional devices. These potential benefits provide a promising direction for applying the TPMS structures in carbon capture applications with the packed column.

One of the major challenges in the development of TPMS-based packed columns is the difficulty in manufacturing due to its complicated structure with channels of varying geometry and cross-sections in all directions. Lawrence Livermore National Laboratory (LLNL) recently developed the additive manufacturing (AM) capability to build reactor geometries with highly specific features, which was not realizable with traditional manufacturing approaches. This capability enables us to manufacture the TPMS units for carrying out the experiments in the packed column. To help speed up the prototyping and guide the geometry design, a CFD framework was developed to explore the hydrodynamics and mass transfer performance in these structures. The three geometries Gyroid, Schwarz-D, and Schwarz-P were selected for this study. Each of the three TPMS geometries have two congruent channels. The countercurrent flow was simulated in both channels to see the influence of the geometry's shape and size on the hydrodynamics and mass transfer.

The third generation non-aqueous CO₂ binding organic liquids (CO₂BOL) developed at the Pacific Northwest National Laboratory (PNNL) was used as the solvent in the countercurrent flow simulations. Compared to an aqueous solvent such as monoethanolamine (MEA), CO₂BOL has lower surface tension and higher viscosity[5]. The established model helped better understand the CO₂BOL behavior in the TPMS structure, which is not yet available in the open literature.

The methodology for carrying out the counterflow simulations in the TPMS is described in Section 2. In Section 3, the simulation results for the three selected geometries are visualized and discussed. The conclusion and future works are provided in Section 4.

2 Methodology

2.1 Geometries

A TPMS is infinite and periodic in three independent directions with a zero mean surface curvature $\kappa = (\kappa_1 + \kappa_2)/2$ at every surface point [6]. The TPMS partitions the space into two intertwining independent regions, while the TPMS surfaces' normal directions are locally changing in space in all directions. The surface structure of the three selected TPMS geometries are approximated by the equations [7]

$$\text{Gyroid} : F(x, y, z) = \cos(x)\sin(y) + \cos(y)\sin(z) + \cos(z)\sin(x) = 0, \quad (1)$$

$$\text{Schwarz-D} : F(x, y, z) = \cos(x)\cos(y)\cos(z) - \sin(x)\sin(y)\sin(z) = 0, \quad (2)$$

$$\text{Schwarz-P} : F(x, y, z) = \cos(x) + \cos(y) + \cos(z) = 0. \quad (3)$$

The TPMS packing walls are then created by offsetting the surface in two opposite directions [2]

$$F_{\text{offset}}(x, y, z) = F(x \pm a_x, y \pm a_y, z \pm a_z), \quad (4)$$

where $a_x = t \frac{F_x}{\sqrt{F_x^2 + F_y^2 + F_z^2}}$, $a_y = t \frac{F_y}{\sqrt{F_x^2 + F_y^2 + F_z^2}}$, $a_z = t \frac{F_z}{\sqrt{F_x^2 + F_y^2 + F_z^2}}$. Examples of TPMS

packing walls used for countercurrent flow simulations are shown in Fig. 2.1. For each geometry shape, there are two unit cells arranged in each direction with a total of 8 repeated unit cells in space. The unit cell is the smallest repeating structure in the TPMS.

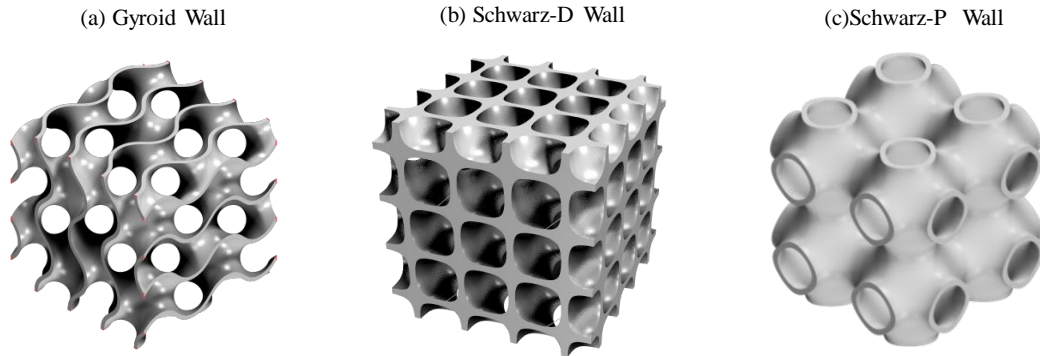


Fig. 2.1 Shape of three TPMS structure packing walls (a) Gyroid, (b) Schwarz-D and (c) Schwarz-P used in this study.

With these given packing walls, the computational domain was generated and meshed by subtracting the walls in the occupied regions. The generated flow channels for simulation are visualized in Fig. 2.2. For each TPMS structure, there were two similarly shaped, independent flow channels created in the computational domain for countercurrent flow simulation. The generated channel was scaled to two different unit cell size (1 cm and 2 cm). The two different unit cell size set up was used to investigate the impact of the TPMS packing size on the hydrodynamics and the mass transfer performance. The 1-cm unit cell size geometry has a total volume of 8 cm³. Dividing the flow channel volume by the total occupied volume, the TPMS geometry porosity ϵ was calculated. The generated Schwarz-P structure had the largest porosity of $\epsilon = 89\%$. The Gyroid had the porosity $\epsilon = 87\%$, and the Schwarz-D had the porosity of $\epsilon = 77\%$. The total occupied volume of the 2-cm unit size geometry was $6.4 \times 10^{-5} \text{ m}^3$ and the porosity of each TPMS was unchanged. More detailed geometry properties of the Gyroid, Schwarz-D, and Schwarz-P are summarized in Table 2.1. The specific area a_p is defined as the channel wall area divided by total volume. The wall thickness of the TPMS structures was estimated by dividing the structure wall's occupied volume by the wall's area. Two kinds of diameters are calculated in the table. The hydraulic diameter d_h is a common term used for determining the pressure drop in the packed column, which is defined as

$$d_h = \frac{4\epsilon}{a_p}. \quad (5)$$

The particle diameter d_p is defined as

$$d_p = \frac{6(1-\epsilon)}{a_p}, \quad (6)$$

which is an alternative way to describe the packing geometry size.

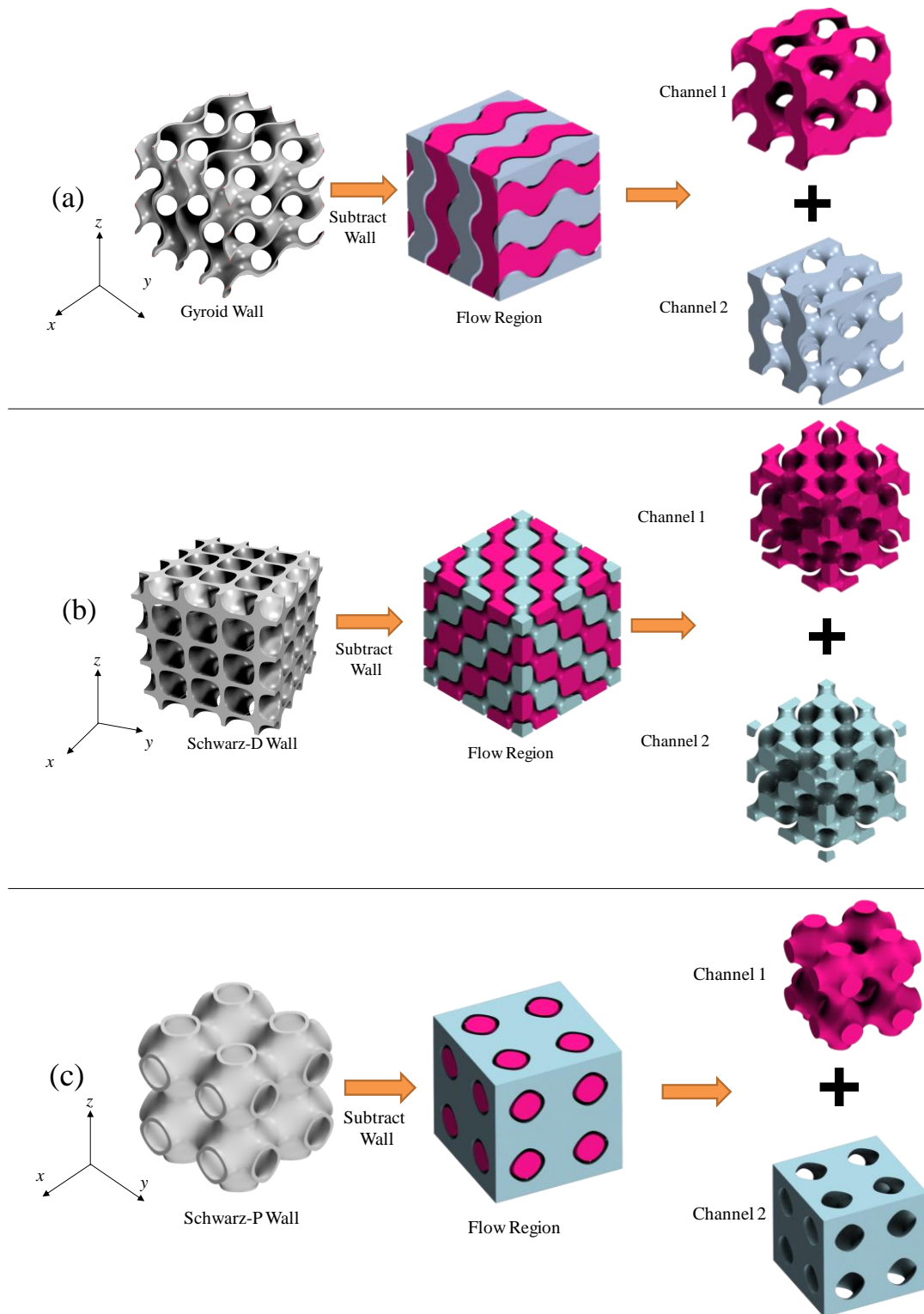
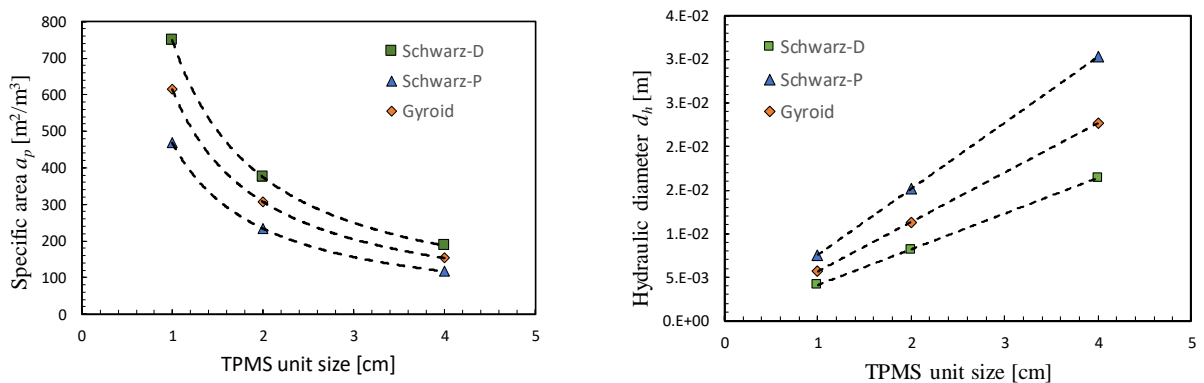


Fig. 2.2 Examples of creating two independent flow channels from the TPMS structure by subtracting the geometry walls.

Table 2.1 Summary of geometry properties of 1-cm and 2-cm unit size Gyroid, Schwarz-D, and Schwarz-P.

Geometry	Schwarz-P		Schwarz-D		Gyroid	
	1	2	1	2	1	2
Unit Size [cm]	1	2	1	2	1	2
Units	2x2x2	2x2x2	2x2x2	2x2x2	2x2x2	2x2x2
Total Volume [m ³]	8.00E-06	6.40E-05	8.00E-06	6.40E-05	8.00E-06	6.40E-05
Wall Thickness [mm]	0.49	0.98	0.62	1.24	0.42	0.84
Specific Area a_p [1/m]	467.38	233.71	748.02	374.10	613.61	306.84
Porosity ϵ [%]	89%	89%	77%	77%	87%	87%
d_h [m]	7.58E-03	1.52E-02	4.10E-03	8.21E-03	5.67E-03	1.13E-02
d_p [m]	1.47E-03	2.94E-03	1.87E-03	3.73E-03	1.27E-03	2.53E-03

Within these parameters, the specific area a_p and hydraulic diameter d_h were closely related to the mass transfer area and packed column pressure drop, respectively. The influence of the unit cell size on these two parameters are plotted in Fig. 2.3. As shown in the figure, the TPMS specific area a_p was inversely proportional to the geometry unit cell size. The Schwarz-D has the largest a_p , followed by Gyroid. The Schwarz-P has the smallest a_p among the three TPMS structures. The hydraulic diameter d_h is linearly proportional to the unit cell size. The Schwarz-P has the largest hydraulic diameter, and the Schwarz-D has the smallest d_h among the three geometries.

Fig. 2.3 Comparison of specific area a_p and hydraulic diameter d_h of Gyroid, Schwarz-D, and Schwarz-P.

2.2 Mathematical Formulations

Countercurrent multiphase flow simulations in the TPMS were performed using the volume of fluid (VOF) method. The continuity and momentum equations are given as follows:

$$\frac{\partial \rho}{\partial t} + \nabla \cdot \rho \mathbf{u} = 0, \quad (7)$$

$$\frac{\partial(\rho \mathbf{u})}{\partial t} + \nabla \cdot (\rho \mathbf{u} \mathbf{u}) = -\nabla p + \mu \nabla^2 \mathbf{u} + \rho \mathbf{g} + \mathbf{F}_\sigma, \quad (8)$$

where ρ is density, μ is viscosity, \mathbf{u} is velocity, p is pressure, and \mathbf{g} is gravity. The terms ρ and μ are phase average quantities that can be computed on the weights of void fraction α .

$$\begin{aligned} \rho &= \rho_g + \alpha(\rho_l - \rho_g), \\ \mu &= \mu_g + \alpha(\mu_l - \mu_g). \end{aligned} \quad (9)$$

The subscript l and g stand for liquid and gas phase, respectively. \mathbf{F}_σ is the surface tension arising at the gas-liquid interface. The \mathbf{F}_σ term is computed as

$$\mathbf{F}_\sigma = \sigma \kappa \nabla \alpha, \quad (10)$$

where σ is the surface tension coefficient and κ is the local curvature of the interface, which is defined as

$$\kappa = -\nabla \cdot \frac{\nabla \alpha}{|\nabla \alpha|}. \quad (11)$$

In the wall region, the liquid-gas interface orientation is determined by the contact angle θ . The interface normal vector is computed as

$$\hat{n} = -n_w \cos \theta_w + t_w \sin \theta_w, \quad (12)$$

The n_w and t_w are the unit normal and tangential vectors of the near wall interface. The transport of the interface was captured by solving the following equation

$$\frac{\partial \alpha}{\partial t} + \nabla \cdot \mathbf{u} \alpha = 0. \quad (13)$$

For the gas-liquid two-phase system, Eq. (13) was solved only for the one phase, and the volume fraction of the second phase was computed as $(1 - \alpha)$.

2.3 Simulation Setup and Boundary Conditions

The multiphase countercurrent flow simulations were conducted using the commercial software STAR-CCM+ 14.02[8]. The unsteady flow simulations were conducted via an implicit unsteady approach. A physical-time step of $\sim 10^{-4}$ seconds was used in the simulation to satisfy the Courant-Friedrichs-Lewy (CFL) condition (Courant number = 0.50) for stability. In this study, the gas and liquid were treated as incompressible. The Semi-Implicit Method for Pressure-Linked Equations (SIMPLE) was used for pressure correction to enforce the mass conservation. The high-resolution interface capturing (HRIC) scheme was used to better track the sharp gas-liquid interface. This helped to acquire a more accurate interface area for mass transfer calculation. The flow region domain was discretized into polyhedral meshes. Refined prism layers were generated on all the TPMS walls to better capture the boundary liquid film flow. For the 1-cm unit size geometry, the averaged mesh size was around 0.15 mm, which yielded a total mesh of 2.5–4 million. For the larger 2-cm unit cell size geometry, the averaged mesh size was increased to around 0.25 mm, and this setup yielded 5.0–7.5 million meshes in simulation. All the simulations were run on the PNNL Institutional Computing's (PIC) high-performance computing (HPC) cluster. The dual Intel Haswell E5-2670 CPUs are installed in the cluster with 24 cores on each node. Ten nodes of 240 cores were used for the simulations. For the cases with 7.5 million meshes, it took around 6 hours of wall clock time for the simulation to propagate one second in physical time.

The boundary condition setup is demonstrated in Fig. 2.4. The Gyroid is plotted in the figure as an example. The x , y , and z directions are all configured with periodic boundary conditions. The solvent is driven by gravity and flows downward. A constant body force of 100 N/m^3 was applied upward on the gas phase, which created the countercurrent flow in the computational domain for both flow channels. The solvent was initialized as a uniform liquid film on the structure walls. An example is plotted in Fig. 2.4(b) at the vertical cross-section plane in the Gyroid flow channel. The blue color stands for the liquid phase. The gray region represents the gas phase and the white region stands for the structure walls. In the following section, the same color conventions are used for countercurrent flow visualization.

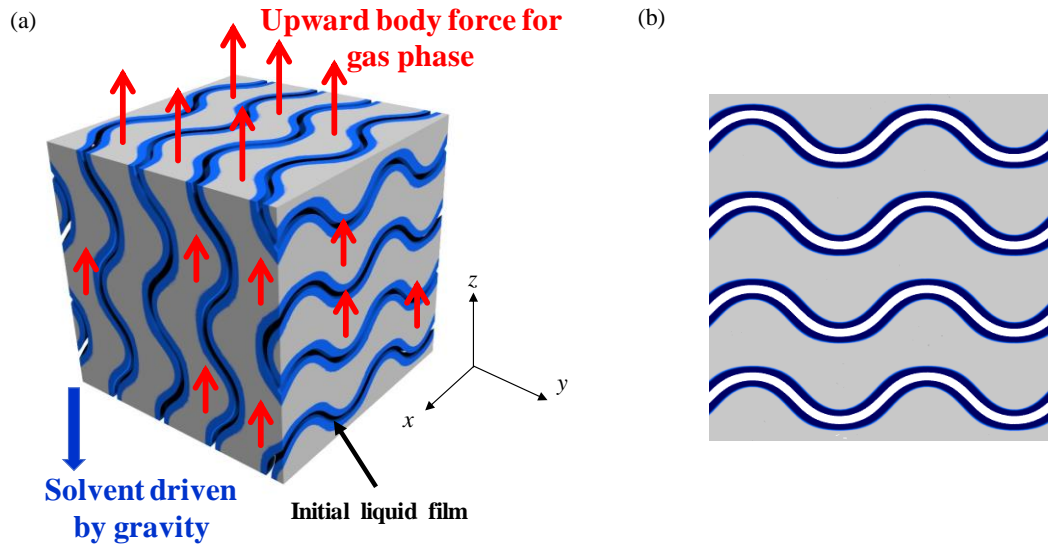


Fig. 2.4 (a) Schematic of the simulation setup using the Gyroid flow region as an example. The solvent is driven by gravity and an upward body force is applied to the gas phase. (b) The initial liquid film distribution visualized at the vertical cross-section plane ($y = 1$ cm) for a 2-cm unit size Gyroid.

The physical properties of the solvent and gas are listed in Table 2.2. The 3rd generation CO₂BOL developed at PNNL was used as the solvent in the simulation[5], [9], [10]. The CO₂BOL is a novel non-aqueous polarity-swing solvent with a reduced energy penalty compared to traditional aqueous solvents. The solvent properties were measured at 40°C with CO₂ loading smaller than 0.05 mol-CO₂/mol-BOL. The stand air properties at 25 °C and 1 atm were used as the gas phase properties.

Table 2.2 Summary of solvent and gas physical properties.

Solvent (3 rd Gen CO ₂ BOL)	Density ρ [kg/m ³]	937.7
	Viscosity μ [cP]	7.1
	Surface Tension σ [N/m]	0.034
	Contact angle [°]	40
Gas Properties (Air)	Density ρ [kg/m ³]	1.184
	Viscosity μ [cP]	0.0186

Due to the constant channel diameter, shape change, and the countercurrent flow oscillation, the simulation generally could not achieve fully steady-state condition. A transient plot example of liquid flow rate and interfacial/wetted area is given in Fig. 2.5. The data was sampled from the 1-cm unit cell size Schwarz-D geometry with an initial film thickness of 0.7mm. In the plot, the liquid flow rate, interface area, and the wetted area show a periodic and repeated fluctuation after the flow developed for around 1 second. No steady-state could be reached. Along with the transient data, the time averaged (over 0.3 seconds) results were also computed in the plots to reduce the impact of instantaneous fluctuations on the results. The following section's results are all reported using the time-averaged data rather than the transient instantaneous readings. All the simulations were run to at least 1s or till the time-averaged flow rate reached a stable condition.

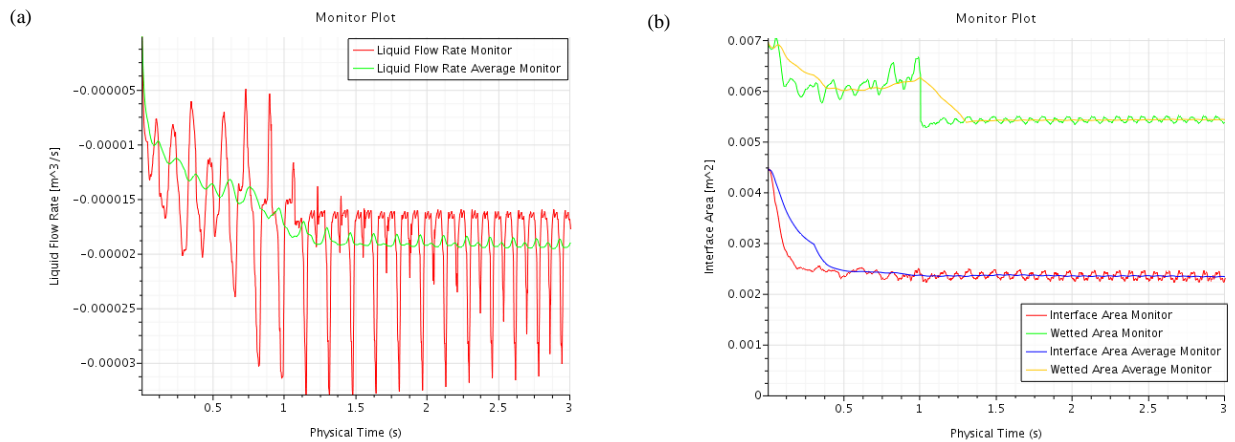


Fig. 2.5 Transient plot of (a) liquid flow rate and (b) interface/wetted area in the 1 cm Schwarz-D structure with the initial liquid film thickness of 0.7 mm.

3 Results and Discussions

3.1 Gyroid Results

The 1-cm unit size Gyroid simulation results are summarized in the Table 3.1. The solvent velocity is defined as cross-sectional superficial velocity

$$u_L = Q / A_{\text{cross}}, \quad (14)$$

where Q is the liquid flow rate and the A_{cross} is the cross-section area. The area is calculated using the cross-section plane which is perpendicular to the z direction. For the 1-cm unit size geometry, the cross-section area is $A_{\text{cross}} = 4 \times 10^{-4} \text{ m}^2$. For the 2-cm unit size geometry, the cross-section area is $A_{\text{cross}} = 1.6 \times 10^{-3} \text{ m}^2$. The interfacial area concentration a_i is defined as

$$a_i = A_i / V, \quad (15)$$

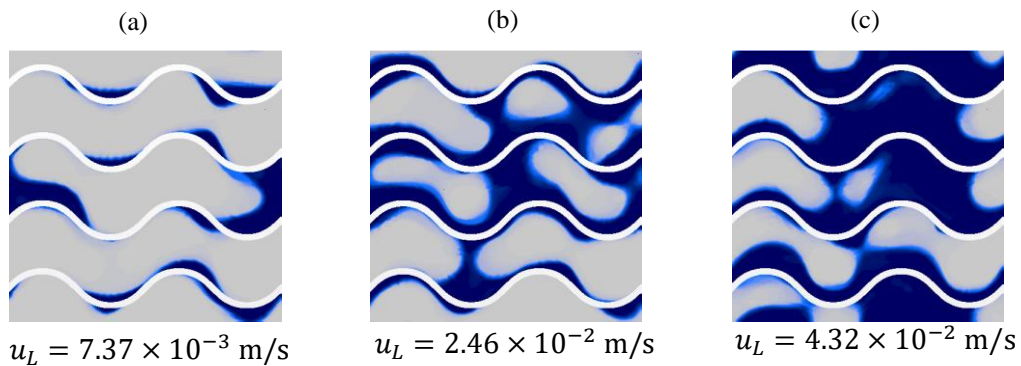
where A_i is the total gas-liquid interface area and V is the total structure occupied volume. Similarly, the wetted area concentration is defined as

$$a_w = A_w / V, \quad (16)$$

where A_w is the total wetted area with void fraction $\alpha > 0.5$ on the TPMS walls. The initial liquid film thickness had the range of [0.2, 0.9] mm, which corresponds to a solvent velocity of $u_L = [0.007, 0.046]$ m/s. With the increase of solvent velocity u_L , both the interfacial area and wetted area increased accordingly. At high velocity $u_L = 4.62 \times 10^{-2}$ m/s, a drop of a_i was observed. For the wetted area, no decreased trend was observed throughout the test solvent velocity range. As the solvent velocity increases, the channel can be partially blocked by the solvent. This can decrease the interfacial area a_i without affecting the wetted area on the structure's surface. Snapshots of countercurrent flow patterns are visualized in Fig. 3.1 at the solvent velocity of $u_L = 7.37 \times 10^{-3}$, 2.46×10^{-2} and 4.32×10^{-2} m/s, respectively. The vertical cross-section plane is located at $y = 0.5$ cm. The flow patterns shown in the images also provide the evidence of the a_i and a_w trends. With small u_L , the liquid film could not fully cover the structure walls, which resulted in a small a_i and a_w compared to the specific area a_p . At large solvent velocity, the solvent spread widely on the structure's walls, which caused the increase of a_w . At the same time, the liquid-gas interface became wavier and, in some regions, the channel was blocked, which resulted in a decrease of a_i at high solvent velocity.

Table 3.1 Summary of simulation results with 1-cm unit size Gyroid with $a_p = 613.76 \text{ m}^2/\text{m}^3$.

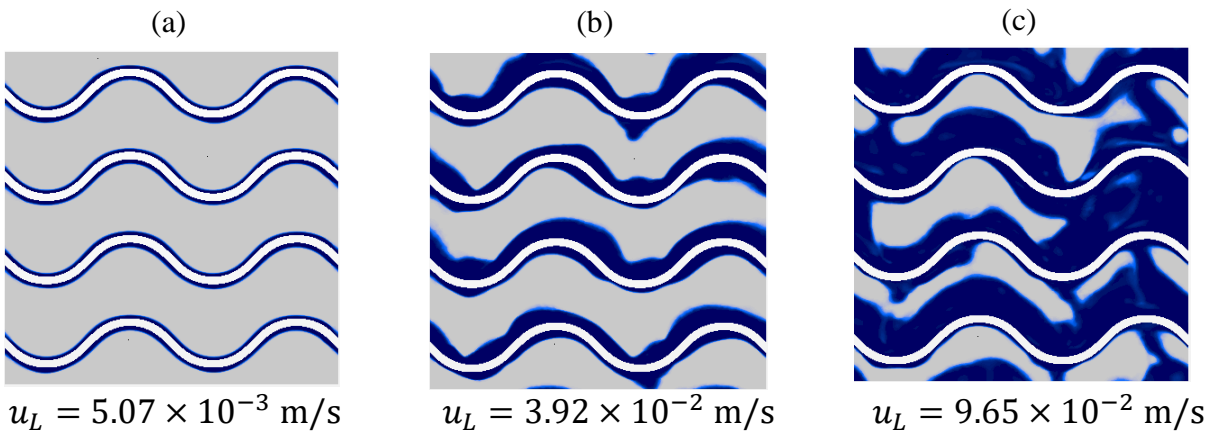
Geometry	Unit Size	Units	Porosity	Initial Film Thickness	a_i	a_w	u_L
	[cm]	Units	[%]	[mm]	$[\text{m}^2/\text{m}^3]$	$[\text{m}^2/\text{m}^3]$	[m/s]
Gyroid	1	2x2x2	0.87	0.2	297.71	236.22	7.37E-03
Gyroid	1	2x2x2	0.87	0.35	388.62	327.40	1.58E-02
Gyroid	1	2x2x2	0.87	0.5	501.25	468.75	3.48E-02
Gyroid	1	2x2x2	0.87	0.7	522.50	522.75	3.89E-02
Gyroid	1	2x2x2	0.87	0.9	490.00	540.01	4.62E-02

Fig. 3.1 Flow pattern visualization with 1-cm unit size Gyroid at vertical cross-section plan $y = 0.5 \text{ cm}$ and solvent flow rate of (a) $u_L = 7.37\text{E-}03$, (b) $2.46\text{E-}2$, and (c) $4.32\text{E-}2 \text{ m/s}$.

For the 2-cm unit size Gyroid, the specific area a_p and hydraulic diameter d_h decreased to half of the 1-cm unit size Gyroid while the porosity remained unchanged. The simulation results for the 2-cm unit size Gyroid are summarized in Table 3.2. The solvent velocity has the range of $[0.005, 0.097] \text{ m/s}$, with the initial film thickness ranging from 0.15 mm to 1.8 mm. Snapshots of flow patterns at the vertical cross-section plane ($y = 1 \text{ cm}$) are visualized at $u_L = 5.07 \times 10^{-3}$, 3.92×10^{-2} and $9.65 \times 10^{-2} \text{ m/s}$ in Fig. 3.2. For low solvent velocity as shown in Fig. 3.2(a), the liquid film was more stable compared to the 1-cm unit size Gyroid. The liquid film covered the Gyroid wall uniformly with no observed liquid film break up. Further increasing the liquid film to 1 mm increased the solvent flow to $3.92 \times 10^{-2} \text{ m/s}$ and the Gyroid wall was still covered by the solvent. It was observed that the gas-liquid film became wavier compared to at a low flow rate, and the liquid film was thicker on the channel wall bottom compared to the channel top surface. Local blockage was also observed at a high solvent flow rate. By blockage henceforth, we refer to the situation at which the fluid flow locally occupies completely the channel and there is no space available for gas flow.

Table 3.2 Summary of simulation results with 2-cm unit size Gyroid with $a_p = 306.84 \text{ m}^2/\text{m}^3$.

Geometry	Unit size	Units	Porosity	Initial Film Thickness	a_i	a_w	u_L
	[cm]	Units	[%]	[mm]	$[\text{m}^2/\text{m}^3]$	$[\text{m}^2/\text{m}^3]$	[m/s]
Gyroid	2	2x2x2	0.87	0.15	160.49	110.42	5.07E-03
Gyroid	2	2x2x2	0.87	0.75	324.59	306.77	2.55E-02
Gyroid	2	2x2x2	0.87	1.0	324.90	306.52	3.92E-02
Gyroid	2	2x2x2	0.87	1.4	316.36	303.18	6.94E-02
Gyroid	2	2x2x2	0.87	1.8	293.67	302.64	9.65E-02

Fig. 3.2 Flow pattern visualization with 2-cm unit size Gyroid at vertical cross-section plan $y = 0.5$ cm and solvent flow rate of (a) $u_L = 5.07\text{E-}03$, (b) $3.92\text{E-}2$, and (c) $9.65\text{E-}2$ m/s.

3.2 Schwarz-D Results

For Schwarz-D, the 1-cm unit size geometry was simulated with an initial film thickness from 0.1 mm to 0.9 mm. This corresponds to the solvent velocity of $u_L = [0.001, 0.06]$ m/s. The simulation data are summarized in

Table 3.3. The a_i increased with u_L at small velocity. For $u_L > 0.01$ m/s, the a_i became relatively stable at around $300 \text{ m}^2/\text{m}^3$ and a slow decrease happened at u_L around 0.055 m/s. Three snapshots with different solvent velocity are visualized in Fig. 3.3 at the horizontal vertical cross-section plane $y = 1$ cm. For small u_L , the Schwarz-D wall was not fully covered by the solvent. The solvent appeared in part of the flow channels, as visualized in the cross-section plane in Fig. 3.3 (a). For high u_L , the wetted area a_w came close

to the specific area a_p . Some part of the channel was fully blocked by the solvent, which resulted in a decrease of liquid-gas interface area at large u_L .

Table 3.3 Summary of simulation results with 1-cm unit size Schwarz-D with $a_p = 748.02 \text{ m}^2/\text{m}^3$.

Geometry	Unit size	Units	Porosity	Initial Film Thickness	a_i	a_w	u_L
	[cm]	Units	[%]	[mm]	$[\text{m}^2/\text{m}^3]$	$[\text{m}^2/\text{m}^3]$	[m/s]
Schwarz-D	1	2x2x2	0.77	0.1	150.68	171.25	1.29E-03
Schwarz-D	1	2x2x2	0.77	0.2	244.39	293.75	4.93E-03
Schwarz-D	1	2x2x2	0.77	0.3	284.25	396.50	8.84E-03
Schwarz-D	1	2x2x2	0.77	0.4	293.88	469.53	1.77E-02
Schwarz-D	1	2x2x2	0.77	0.5	304.40	526.25	2.22E-02
Schwarz-D	1	2x2x2	0.77	0.6	307.98	588.75	2.43E-02
Schwarz-D	1	2x2x2	0.77	0.7	293.75	679.95	4.82E-02
Schwarz-D	1	2x2x3	0.77	0.9	266.59	727.50	5.53E-02

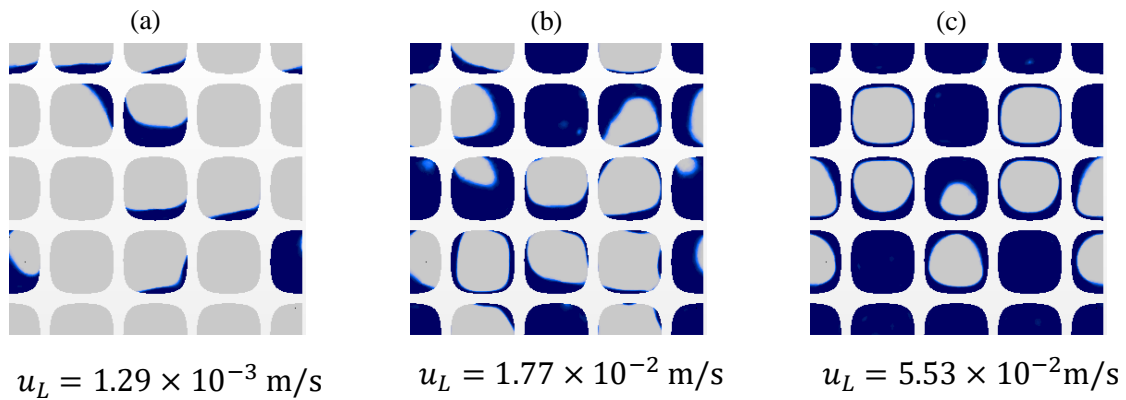


Fig. 3.3 Flow pattern visualization with 1-cm unit size Schwarz-D at vertical cross-section plan $y = 1$ cm and solvent flow rate of (a) $u_L = 1.29\text{E-}03$, (b) $1.77\text{E-}2$, and (c) $5.53\text{E-}2$ m/s.

For the 2-cm unit size Schwarz-D geometry, the porosity remained unchanged and the specific area a_p decreased to half of the 1-cm unit size geometry. With the initial film thickness of 0.2 to 1.1 mm, the solvent velocity has the range of $[0.0035, 0.076]$ m/s. The simulation results are summarized in Table 3.4. Flow patterns are visualized at three different u_L in Fig. 3.4. The vertical cross-section plane was extracted at $y = 2$ cm. Compared to the 1-cm unit size geometry, the solvent distributed more uniformly in all the

channels. For small u_L , the solvent mostly deposited at the bottom of the channel. Increasing the u_L further covered the side of the channel by the solvent and no blockage was observed for the solvent velocity up to 0.076 m/s.

Table 3.4 Summary of simulation results with 2-cm unit size Schwarz-D with $a_p = 374.10 \text{ m}^2/\text{m}^3$.

Geometry	Unit size	Units	Porosity	Initial Film Thickness	a_i	a_w	u_L
	[cm]	Units	[%]	[mm]	$[\text{m}^2/\text{m}^3]$	$[\text{m}^2/\text{m}^3]$	[m/s]
Schwarz-D	2	2x2x2	0.77	0.2	135.47	137.59	3.45E-03
Schwarz-D	2	2x2x2	0.77	0.3	158.42	163.46	7.56E-03
Schwarz-D	2	2x2x2	0.77	0.5	195.17	203.73	1.97E-02
Schwarz-D	2	2x2x2	0.77	0.7	203.64	224.28	3.49E-02
Schwarz-D	2	2x2x2	0.77	0.9	212.49	247.00	5.64E-02
Schwarz-D	2	2x2x2	0.77	1.0	217.56	256.73	6.41E-02
Schwarz-D	2	2x2x2	0.77	1.1	219.94	266.34	7.59E-02

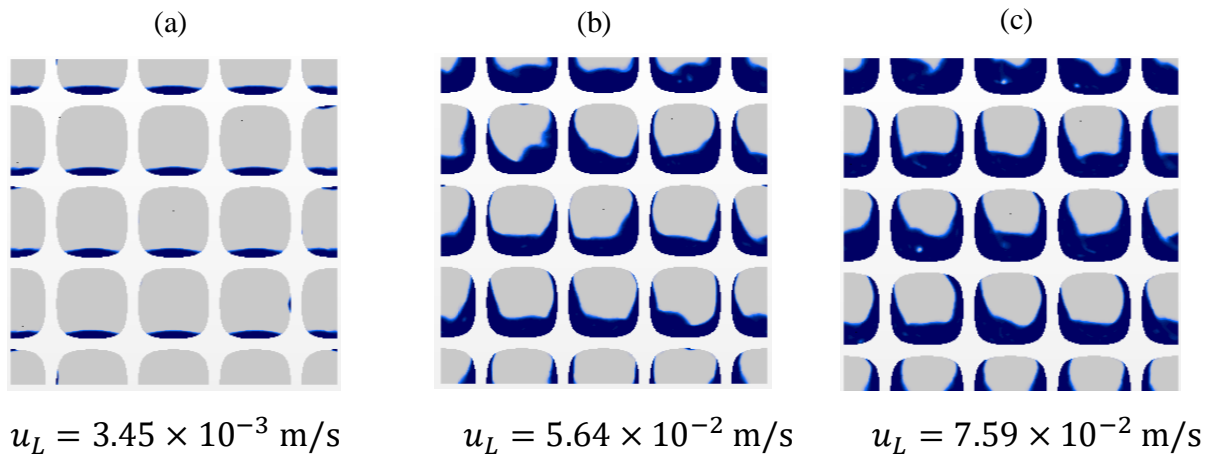


Fig. 3.4 Flow pattern visualization of 2-cm unit size Schwarz-D at vertical cross-section plan $y = 2$ cm and solvent flow rate of (a) $u_L = 3.45\text{E-}03$, (b) $5.64\text{E-}2$, and (c) $7.59\text{E-}2$ m/s.

3.3 Schwarz-P Results

Following the same structure presented in the previous two sections, both the 1-cm and 2-cm unit size Schwarz-P simulation results are summarized in this section. The 1-cm unit size Schwarz-P results are summarized in Table 3.5 and the 2-cm unit size Schwarz-P results are summarized in Table 3.6. For the 1-cm unit size Schwarz-P, the initial film thickness has the range of [0.1, 1] mm with the corresponding solvent velocity of [0.002, 0.057] m/s. For the 2-cm unit size Schwarz-P, the initial film thickness has the

range of [0.2 1.5] mm with the corresponding solvent velocity of [0.003 0.087] m/s. For both the 1-cm and 2-cm unit size geometry, the a_i increased with u_L at small velocity. At large velocity, local flow blockage and bridged liquid film were observed for the 1-cm unit, as shown in Fig. 3.5. This resulted in a decrease of a_i at larger u_L . The wetted area thus became larger than the interfacial area at high u_L cases. For the 2-cm unit, the a_i had a slow increase with $u_L > 0.088$ m/s. The flow structures are visualized in Fig. 3.6 at the vertical cross-section of $y = 1$ cm. The 2-cm unit has a larger hydraulic diameter d_h and is less prone to be blocked by solvent. The larger size channel provided a space for the entrainment of the liquid droplet and the formation of the free streams, which contributed to the increase of the interfacial area a_i .

Table 3.5 Summary of simulation results with 1-cm unit size Schwarz-P with $a_p = 467.38 \text{ m}^2/\text{m}^3$.

Geometry	Unit Size	Units	Porosity	Initial Film Thickness	a_i	a_w	u_L
	[cm]	Units	[%]	[mm]	$[\text{m}^2/\text{m}^3]$	$[\text{m}^2/\text{m}^3]$	[m/s]
Schwarz-P	1	2x2x2	0.89	0.1	125.60	120.28	2.06E-03
Schwarz-P	1	2x2x2	0.89	0.175	138.70	141.51	6.99E-03
Schwarz-P	1	2x2x2	0.89	0.25	190.718	198.78	1.07E-02
Schwarz-P	1	2x2x2	0.89	0.5	440.61	467.38	1.61E-02
Schwarz-P	1	2x2x2	0.89	0.9	413.06	465.78	3.80E-02
Schwarz-P	1	2x2x3	0.89	1.0	325.97	409.84	5.68E-02

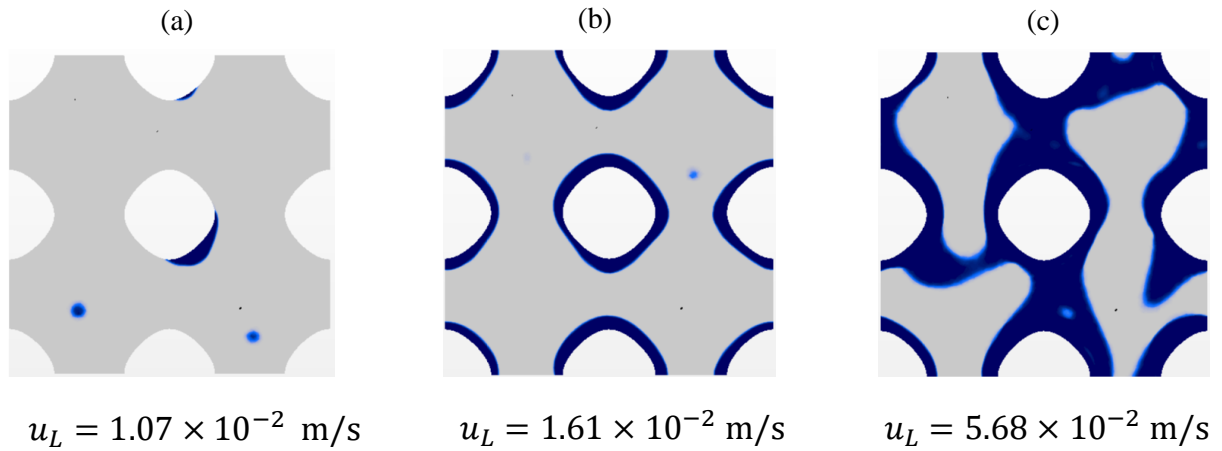
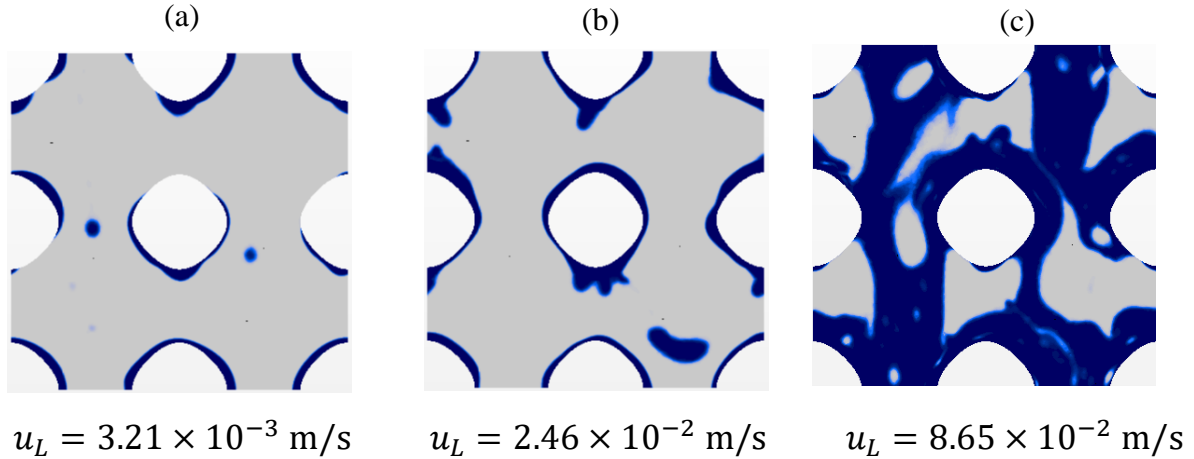


Fig. 3.5 Flow pattern visualization of 1-cm unit size Schwarz-P at vertical cross-section plan $y = 0.5$ cm and solvent flow rate of (a) $u_L = 1.07\text{E-}02$, (b) $1.61\text{E-}2$, and (c) $5.68\text{E-}2$ m/s.

Table 3.6 Summary of simulation results with 2-cm unit size Schwarz-P with $a_p = 233.71 \text{ m}^2/\text{m}^3$.

Geometry	Unit Size	Units	Porosity	Initial Film Thickness	a_i	a_w	u_L
	[cm]	Units	[%]	[mm]	$[\text{m}^2/\text{m}^3]$	$[\text{m}^2/\text{m}^3]$	[m/s]
Schwarz-P	2	2x2x2	0.89	0.2	96.60	91.61	3.21E-03
Schwarz-P	2	2x2x2	0.89	0.5	210.32	212.87	8.83E-03
Schwarz-P	2	2x2x2	0.89	0.8	235.64	233.59	2.46E-02
Schwarz-P	2	2x2x2	0.89	1	242.13	233.44	4.34E-02
Schwarz-P	2	2x2x2	0.89	1.5	275.48	231.96	8.65E-02

Fig. 3.6 Flow pattern visualization of 2-cm unit size Schwarz-P at vertical cross-section plan $y = 1$ cm and solvent flow rate of (a) $u_L = 3.21\text{E-}03$, (b) $2.46\text{E-}2$, and (c) $8.635\text{E-}2$ m/s.

3.4 Discussion and Analysis of Results.

To find out the TPMS size optimization strategies maximizing the interfacial area a_i for mass transfer, the interfacial area a_i was compared with a different unit size, as shown in Fig. 3.7 and Fig. 3.8. It is observed that a small unit size structure generally has a large chance of being partially blocked by the solvent with the increase of solvent flow rate. Therefore, the normalized $a_{i,\text{norm}}$ defined as the ratio of the interface and the specific areas, would be smaller for small unit size TPMS, and the utilization of the wall area would be less efficient. However, small unit size TPMS has a larger absolute interfacial area a_i value for mass transfer, even blockages can happen in the channels. The performance of the three geometries was also compared with the same unit size as shown in Fig. 3.9. For both 1-cm and 2-cm unit size geometry, Gyroid has the largest interfacial area at the same solvent velocity u_L . The Schwarz-P ranked second among the three geometries. The Schwarz-D has the smallest interfacial area a_i even though it has the largest a_p . One possible reason is that the Schwarz-D has the smallest hydraulic diameter d_h among the three structures,

given same unit size configuration. The blockage and liquid breakup can happen more easily in Schwarz-D with a smaller channel size, which resulted in a smaller a_i compared to the Gyroid and Schwarz-P units.

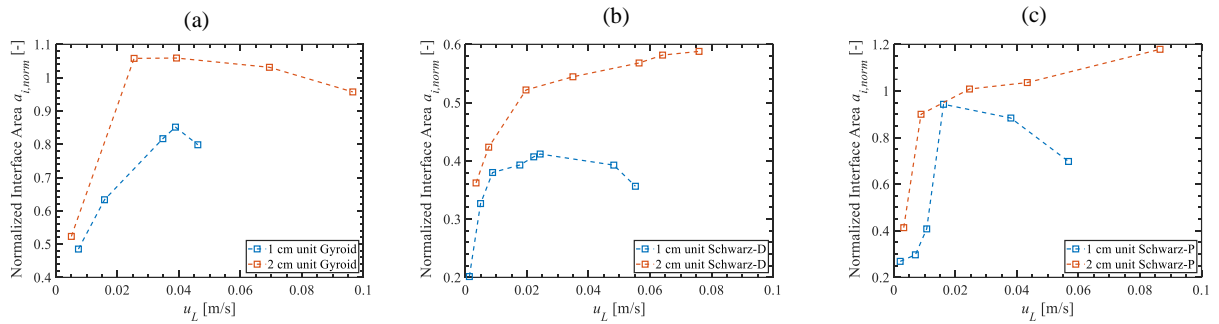


Fig. 3.7 Comparison of how the geometry size affects the normalized interfacial area $a_{i, norm}$ for (a) Gyroid, (b) Schwarz-D, and (c) Schwarz-P.

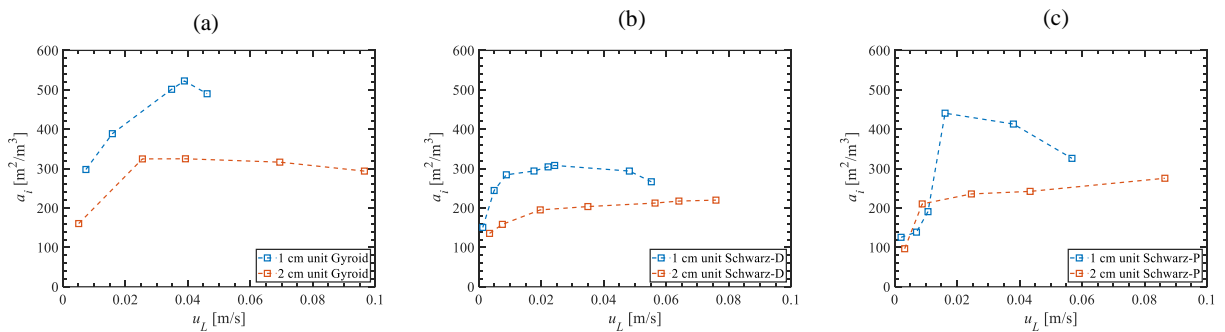


Fig. 3.8 Comparison of how the geometry size affects the interfacial area a_i for (a) Gyroid, (b) Schwarz-D, and (c) Schwarz-P.

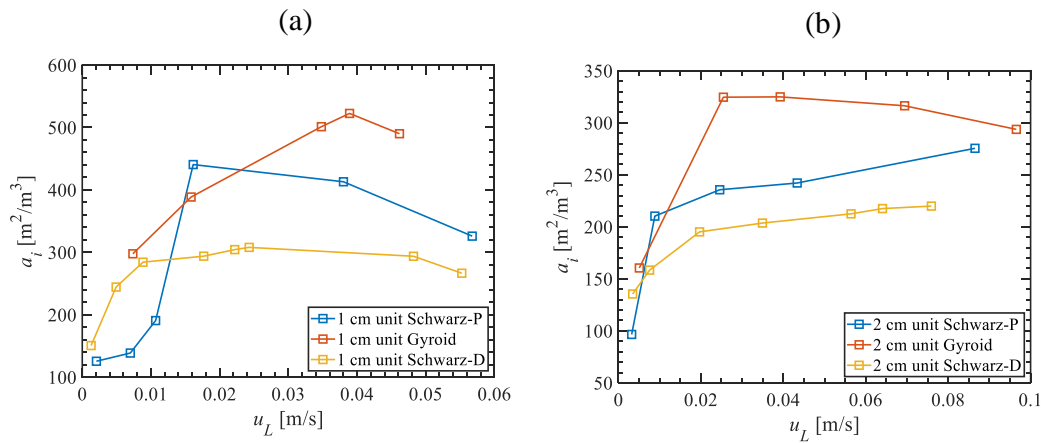


Fig. 3.9 Comparison of the interfacial area a_i among Gyroid, Schwarz-D, and Schwarz-P with (1) 1-cm unit size geometry and (2) 2-cm unit size geometry.

4 Conclusions

This study established a CFD framework to carry out countercurrent flow simulations in the TPMS structures. The developed CFD tools help speed up the TPMS structure prototype using the AM and optimize the TPMS geometries for enhanced mass transfer efficiency. Three geometries, Gyroid, Schwarz-D, and Schwarz-P, were investigated in this report with the novel non-aqueous solvent CO₂BOL developed at PNNL. The 1-cm and 2-cm units were explored to find the impact of geometry size on the TPMS hydrodynamics and mass transfer area. The studied solvent velocity covered the range of [0, 0.06] m/s for 1-cm unit size geometry. For the 2-cm unit, the solvent velocity covered a range of [0, 0.1] m/s. The major findings are summarized in the following list:

1. 1-cm unit size TPMS has a smaller normalized interface area $a_{i,\text{norm}}$, which results in low efficiency in utilizing the packing walls. However, small unit size (1 cm) geometry can have larger absolute interfacial area a_i for mass transfer compared to large unit size (2 cm) structures.
2. The solvent velocity is recommended to operate at $u_L > 0.02$ m/s for better wetting the structure walls for optimized mass transfer performance.
3. Different factors are found to affect the interfacial area a_i in the countercurrent flow in TPMS. Flow channel blockage and liquid film breakup are the most common reasons for decreasing the a_i . Entrained droplets and free streams at high u_L can be the reasons for increased a_i , provided that no blockage happens.
4. For both 1-cm and 2-cm unit size TPMS geometries, the interfacial area a_i has a rank of Schwarz-D < Schwarz-P < Gyroid at the same solvent velocity.

5 Future Work

Overall, this report provides the preliminary results of investigating the performance of three TPMS structures for CO₂ capture tasks. For a more comprehensive understanding of these geometries, future work will be focused on the following directions:

1. One of the fundamental assumptions of this work was the linear nature of the liquid solvent. However a proper investigation should be carried out to verify the linearity in terms of shear stress-strain relationship, shear viscosity, the effects of temperature and concentration (solvent loading and other variables). As we move to models of higher complexity involving absorption reactions, heat and mass transfer, the dependence of the viscosity and of the interfacial phenomena quantified by the surface tension and contact angle on the afore-mentioned factors, might affect the studied hydrodynamic performance as well. Further evaluation should be carried out by varying the aforementioned factors.
2. The simulations will be scaled up to a representative column size with given inlet and outlet boundary conditions. Those models will be more faithful in representing the actual packed column operation conditions and provide further insights on the intensified packed column design and optimization.
3. Current results focus on the non-reacting flow hydrodynamics and mass transfer area prediction. Future work will increase the model scope to include the aspect absorption reactions, heat and mass transfer.
4. More types of TPMS structures will be investigated.

6 References

- [1] J. Mackowiak, *Fluid Dynamics of Packed Columns*. Springer Berlin Heidelberg, 2010.
- [2] T. Femmer, A. J. C. Kuehne, and M. Wessling, “Estimation of the structure dependent performance of 3-D rapid prototyped membranes,” *Chem. Eng. J.*, vol. 273, pp. 438–445, 2015.
- [3] N. Sreedhar *et al.*, “3D printed feed spacers based on triply periodic minimal surfaces for flux enhancement and biofouling mitigation in RO and UF,” *Desalination*, vol. 425, no. September, pp. 12–21, 2018.
- [4] N. Sreedhar *et al.*, “Mass transfer analysis of ultrafiltration using spacers based on triply periodic minimal surfaces: Effects of spacer design, directionality and voidage,” *J. Memb. Sci.*, vol. 561, no. March, pp. 89–98, 2018.
- [5] D. J. Heldebrant, P. K. Koech, V. A. Glezakou, R. Rousseau, D. Malhotra, and D. C. Cantu, “Water-Lean Solvents for Post-Combustion CO₂ Capture: Fundamentals, Uncertainties, Opportunities, and Outlook,” *Chem. Rev.*, vol. 117, no. 14, pp. 9594–9624, 2017.
- [6] M. P. Do Carmo, *Differential Geometry of Curves and Surfaces: Revised and Updated Second Edition*. Courier Dover Publications, 2016.
- [7] P. J. F. Gandy, S. Bardhan, A. L. Mackay, and J. Klinowski, “Nodal surface approximations to the P, G, D and I-WP triply periodic minimal surfaces,” *Chem. Phys. Lett.*, vol. 336, no. 3–4, pp. 187–195, 2001.
- [8] CD-adapco, “STAR-CCM+ 14.02 User Guide.” 2019.
- [9] D. J. Heldebrant *et al.*, “Are Water-lean Solvent Systems Viable for Post-Combustion CO₂ Capture?,” *Energy Procedia*, vol. 114, no. November 2016, pp. 756–763, 2017.
- [10] P. M. Mathias *et al.*, “Measuring the Absorption Rate of CO₂ in Nonaqueous CO₂-Binding Organic Liquid Solvents with a Wetted-Wall Apparatus,” *ChemSusChem*, vol. 8, no. 21, pp. 3617–3625, 2015.